# A high anti-impact STF/Ecoflex composite structure with a sensing capacity for wearable design

Junshuo Zhang, Yu Wang [**], Huaxia Deng, Jianyu Zhou, Shuai Liu, Jianpeng Wu, Min Sang, Xinglong Gong [*]

*CAS Key Laboratory of Mechanical Behavior and Design of Materials, Department of Modern Mechanics, University of Science and Technology of China (USTC), Hefei, 230027, PR China*

## ABSTRACT

By encapsulating shear thickening fluid (STF) in Ecoflex-0030, a kind of composite structure with excellent anti-impact and high energy absorption properties was obtained. The drop hammer tests indicated that the increase of STF concentration could improve the anti-impact and energy absorption capacity of STF/Ecoflex. Furthermore, the loss rate of impact energy of STF/Ecoflex was 63.6% and 36.6% higher than that of aluminum alloy and Kevlar materials, respectively. Numerical simulation was used to explore the mechanism. It was found that the shear thickening effect of STF was enhanced with the increase of STF concentration, which could lead to the increase of the stress level of STF and the energy dissipated by friction and viscosity, thereby the anti-impact performance of the composite was improved. Then, the C-STF/Ecoflex was prepared by adding carbon nanotubes (CNTs) to STF, which had excellent impact sensing function and could be combined with Kevlar for multi-functional wearable devices with anti-impact properties.

## 1. Introduction

Human beings may be injured in situations such as fighting against sports' incidents, natural disasters and dangerous working environments, so it is an emergency task to develop a super suit to withstand violent external shocks [1–4]. Liquid armor composed of ballistic fabric and shear thickening fluid (STF) has attracted much attention in recent years because of its excellent protection and wearing comfort [5–7].

The viscosity of shear thickening fluid (STF) increases sharply with the increase of shear rate or shear stress, and sometimes its state even changes from liquid to solid, resulting in shear jamming [8–10]. In addition to displaying shear thickening under shear conditions, STF can also be observed thickening or plugging under other mechanical conditions, such as vibration [11], tensile [12], high strain rate impact [13], falling ball impact [14], etc. Typical rate-dependent characteristics give STF broad application prospects in many fields, such as polishing [15, 16], damping [17,18], liquid body armor [19–21], etc. Therefore, more and more attention has been paid to the application of STF to improve the anti-impact properties of soft armor [22–29]. Wagner [30] et al. introduced shear thickening fluid (STF) into Kevlar woven fabric for the first time to improve the impact resistance of Kevlar. By comparing the energy absorption capacity of monodispersed STFs and bi-dispersed STFs impregnated Kevlar fabric, Mawkhlieng and Majumdar [31] showed that the shear thickening effect of STF played a leading role in enhancing the impact resistance of the fabric. Khodadadi et al. [32] found that impregnation of STF increased the specific energy absorption (SEA) of the fabric. The SEA in the case of 35. wt% STF/Kevlar composites was 2.3 times larger than those of the neat fabric. After the addition of STF, the impact resistance of the composite is improved obviously, but the thickness, weight and stiffness of the composite are not increased significantly. However, when STF is exposed to air, the shear thickening performance may decrease or even disappear due to water absorption or solvent volatilization. Sealing shear thickened fluids is therefore a challenge faced in the application.

Damage can be detected in the process of resistance to impact, which helps people quickly locate the injured area and accurately judge the degree of injury. As an important part of wearable devices or electronic skin, flexible sensors [33–37] show satisfactory application prospects in human motion detection, health monitoring, soft robots and other aspects. Besides the body protection, the STF also has been proven to be

---

effective in wearable devices. Qin [38] made STF-processed Kevlar fabrics (STKF) by impregnating Kevlar fibers with a new shear thickening fluid composed of silicon microspheres and ionic liquid, which was conductive and its resistance was highly sensitive to the applied deformation. Besides, the electromagnetic interference shielding capacity of the STKF was as high as 27 dB, while the electromagnetic interference shielding capacity of the KF was close to 0 dB. Liu [39] prepared a new wearable electronic textile based on CNT/STF/Kevlar with good protection and electrical conductivity performance, which enabled the composite material to have excellent sensing performance when monitoring human movement under different conditions. Recently, Wang [40] prepared a miniaturized triboelectric Nano generator (TENG) by assembling shear thickening fluid and magnetically sensitive film, which could be used in self-powered sensing devices. In consideration of the outstanding anti-impact performance, the conductive STF with both excellent sensing property and safeguarding performance will be attractive in multifunctional body armor and wearable devices.

In this paper, STF/Ecoflex was prepared by encapsulating STF in Ecoflex. Then, the effect of STF concentration on STF/Ecoflex anti-impact performance was tested, and numerical simulations were also performed to explain the anti-impact mechanism. Finally, by adding CNTs to STF, a multifunctional C-STF/Ecoflex with both anti-impact and sensing properties was prepared, which could be combined with Kevlar fabric as a lining of wearable fabric.

## 2. Materials and methods

### 2.1. Preparation of STFs and STF/Ecoflex composites

The mechanical properties of Kevlar, Silica and Ecoflex were shown in Table 1. The plain weave Kevlar 129 (1.44 g/cm$^3$) was got from Beijing Junantai Protection Technology Co., Ltd. The spherical silica particles with a dimension of 300 ± 100 nm, density of 2.1± 0.1 g/cm$^3$, and a category (Specific surface area) of A were purchased from Shanghai Bu Micro Applied Materials Technology Co., Ltd. The silicone rubber Ecoflex-0030 was purchased from Smooth-On, PA, USA. The ethanol and polyethylene glycol (PEG200) were purchased from Sinopharm Chemical Reagent Co., Ltd, Shanghai, China, and used without further purification. Carbon nanotubes (CNTs) with a length of 3–12 μm were supplied by Kaina Carbon New Material Co., LTD, Xiamen City, Fujian province, China. The 3D fabric was a three-dimensional polyester fiber that has a mesh on both sides, with supporting fibers in the middle perpendicular to the top and bottom. The 3D fabric was 2.5 mm thick and it was commercially available.

The spherical silica particles were used as the dispersed phase, which were added into PEG200 and then put into a ball mill for 24 h at room temperature to prepare STF. The preparation procedure of STF/Ecoflex was as followed. As shown in Fig. 1, firstly, the Ecoflex-0030 (Smooth-On Inc) was poured into the 3D-printed mold followed by curing at 45 °C for 30 min. Then, the Ecoflex films were peeled off as the shell. The 3D fabric was cut into 20 mm × 20 mm × 2.5 mm size pieces and attached onto the Ecoflex shell. The main function of the 3D fabric was to support the upper surface of the sample, preventing formation collapse of Ecoflex film. Then the prepared STF was slowly injected into Ecoflex shell using a syringe until it just passed through the 3D fabric, and then the Ecoflex-0030 was injected into until it was flush with the top edge of the shell. Finally, they were cured at 45 °C for 30 min. The STF/Ecoflex size

**Table 1**
The mechanical properties of Kevlar, Silica and Ecoflex.

| Material | Density | Particle size | Young's Modulus |
|---|---|---|---|
| Kevlar | 1.44 g/cm$^3$ | – | 88 GPa |
| Silica | 2.1 ± 0.1 g/cm$^3$ | 300 ± 100 nm | – |
| Ecoflex-0030 | 1.08 g/cm$^3$ | – | – |

was 23 mm × 23 mm × 5 mm and the size of STF in STF/Ecoflex was 20 mm × 20 mm × 2.5 mm.

### 2.2. Test and analysis methods

#### 2.2.1. Rheological test

The rheological properties of STF were tested using the rheometer (Anton-Paar MCR 302) with cone-plate geometry (20 mm in diameter and 2° in cone angle) under steady shear. All the experiments were conducted with a gap size of 0.085 mm at a room temperature of 25 °C.

#### 2.2.2. Compression test

The compression test was conducted with the universal tensile instrument (MTS Criterion™ Model 43). The sample size was 23 mm × 23 mm × 5 mm. The bottom of the sample was placed in the center of the lower grip of MTS (Fig. 2a). Several experiments with the constant loading speed varying from 0.1, 0.3, 0.5, 1, 1.5, to 2 mm/s were conducted individually, and the force vs. displacement curves were recorded at the same time.

#### 2.2.3. Drop hammer test

The low velocity impact tests of the composites were performed by a drop tower impact tester (Fig. 2b). The bottom of the impactor was a steel cylinder with a diameter of 50 mm. The size of the whole specimen was 23 mm × 23 mm × 5 mm. The sample was placed on the center of the force sensor. A total of 0.64 kg loading dropped freely from the height of 15, 30, 45, 60–75 cm, which equaled to the impact speed from 1.71, 2.42, 2.97, 3.43 to 3.83 m/s, respectively.

#### 2.2.4. Finite element analysis (FEA)

In this research, the process of STF/Ecoflex being impacted by falling hammer was simulated with the coupling Eulerian Lagrange (CEL) method. The finite element (FE) model was created in Abaqus/Explicit. Fig. 2c showed the finite element model of drop hammer impact: An 50 mm diameter rigid hammer head with a mass of 0.64 kg impacting STF/Ecoflex in the normal direction. The STF/Ecoflex sat on top of a rigid plate with a diameter of 50 mm. The Ecoflex-0030 (Lagrangian domain) size was 23 mm × 23 mm × 5 mm, the Eulerian domain size was 60 mm × 60 mm × 5 mm, and the size of STF (Eulerian material) which located in the Ecoflex-0030 was 20 mm × 20 mm × 2.5 mm. The size of the Eulerian domain was larger than that of the Eulerian material to accommodate the large deformation/flow of the Euler material. If any Eulerian material moved outside the Eulerian domain, it would be lost from the simulation. The rigid plate was fixed and the initial impact speed $V_0$ of the hammerhead was 3.43 m/s, which were the boundary conditions of the model.

The hyperelastic constitutive Ogden model was adopted to define the mechanical behaviors of Ecoflex-0030 [41]. The materials parameters $\mu_i$, $\alpha_i$, and $D_i$ used in the model were shown in Table 2. Equation of State (EOS) [42] and shear viscosity were used to define the deformation characteristic of STF. Here, a parameter table (Supplementary information, Section S4) was used to define the shear-rate-dependent viscosity property for STF, which was based on the results of rheological tests. General contact was selected in the simulation and the contact was generated using a hard contact-penalty algorithm provided by the Abaqus/Explicit. The time step type was Dynamic/Explicit and the incrementation type was automatic. There were 246588 C3D8R elements in the Ecoflex model, 722 C3D8R elements in the rigid plate model, 2872 C3D8R elements in the hammer head model, and 1152000 EC3D8R elements in the Eulerian domain.

#### 2.2.5. Electrical performance tests

In this study, two methods were used to collect the changes of resistance signals. First, the resistance change of the sample was directly collected by an impedance meter (Fig. 2d). Because the sampling frequency of the impedance meter was low, it was not suitable to collect the
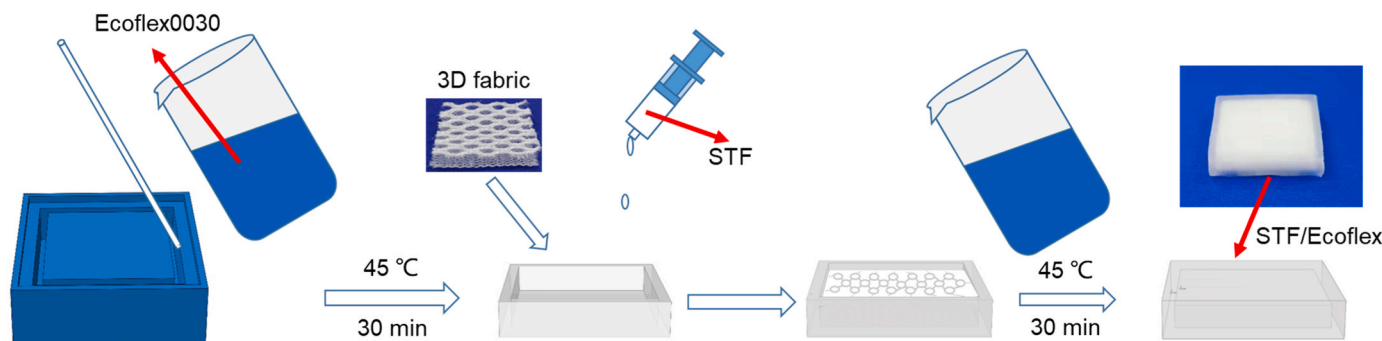
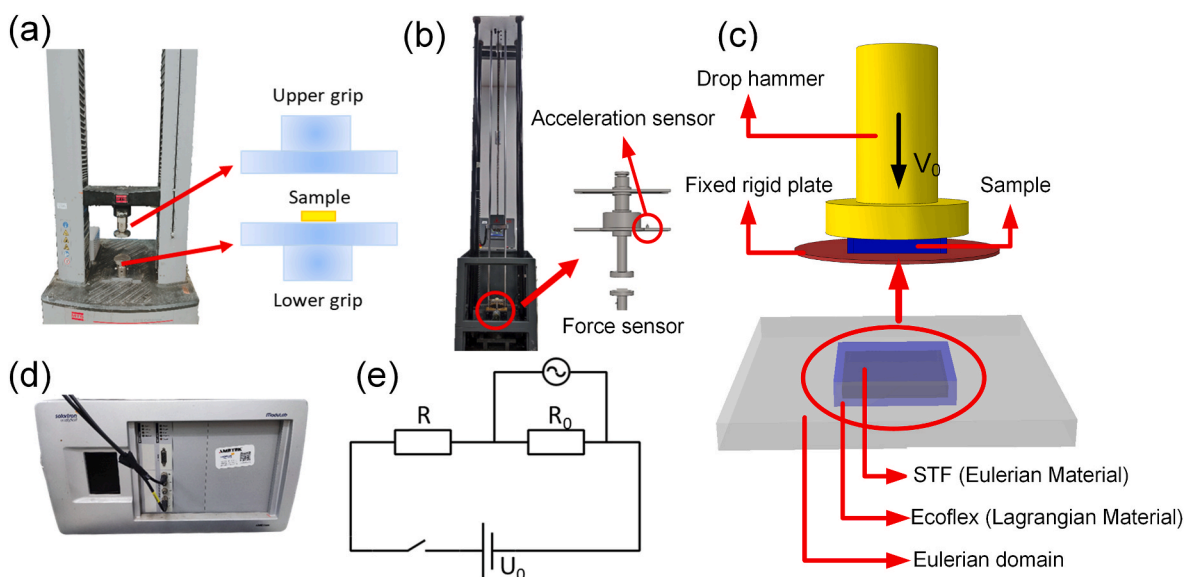**Fig. 1.** Schematic diagram of STF/Ecoflex preparation process.



**Fig. 2.** The experimental equipment of (a) compression test system and (b) drop hammer. (c) Finite element model of drop hammer impact. The experimental equipment of (d) impedance meter. (e) The partial voltage circuit diagram.

**Table 2**
Material Parameters for Ecoflex used in FEA Simulation [41].

| I | $\mu_i$ (kPa) | $\alpha_i$ | $D_i$ |
|---|---|---|---|
| 1 | 16.9 | 1.3 | 1.156 |
| 2 | 0.08 | 5.0 | 0.0001 |
| 3 | 1.0 | −2.0 | – |

resistance signal changes of samples at high frequency. The partial voltage method (Fig. 2e) was used to collect the resistance signal changes of samples at high frequency. A constant resistance with similar resistance value was connected in series to the sample. After the constant voltage power supply was connected, an oscilloscope was used to collect the partial pressure change of the customized resistance. Then the resistance of the sample was:

$$R = \frac{U_0 - U_{R_0}}{U_{R_0}} R_0 \tag{1}$$

where $R_0$ was the customized resistance, $U_{R_0}$ was the partial voltage at both ends of the fixed resistance, and $U_0$ was the power supply voltage. In this paper, the direct measurement method was used for compression tests and the partial voltage method was used for drop hammer and ballistic tests.

## 3. Results and discussion

### 3.1. Characterization and rheological property of STF

First, the microscopic morphological characterization of the material was carried out. The spherical silica particles were monodisperse with an average particle size of about 370 nm (Fig. 3a). As could be seen from Fig. 3b, CNTs were about 22 nm in diameter.

The rheological properties of the shear thickening fluid with different concentrations were tested. As the mass fraction of $SiO_2$ in STF increasing from 56%, 59%, 62%–65%, the critical shear rate decreased from 74.4 $s^{-1}$, 58.8 $s^{-1}$, 36.7 $s^{-1}$ to 2.2 $s^{-1}$, and the maximum viscosity increased from 1.6 Pa·s, 5.9 Pa·s, 31.3 Pa·s to 646.1 Pa·s, respectively (Fig. 3c). Furthermore, the addition of CNTs to STF could improve the shear thickening effect of STF. The addition of CNTs at 1% mass fraction to 62. wt%STF reduced the critical shear rate from 36.7 $s^{-1}$ to 16.0 $s^{-1}$ and increased the peak viscosity from 31.3 Pa·s to 107.7 Pa·s. It could be seen from Fig. 3d that the shear stress and viscosity showed the same growth trend. The mass fraction of $SiO_2$ showed a great influence on the rheological behavior of STF.

### 3.2. The mechanical performance of STF/Ecoflex

#### 3.2.1. Compression tests

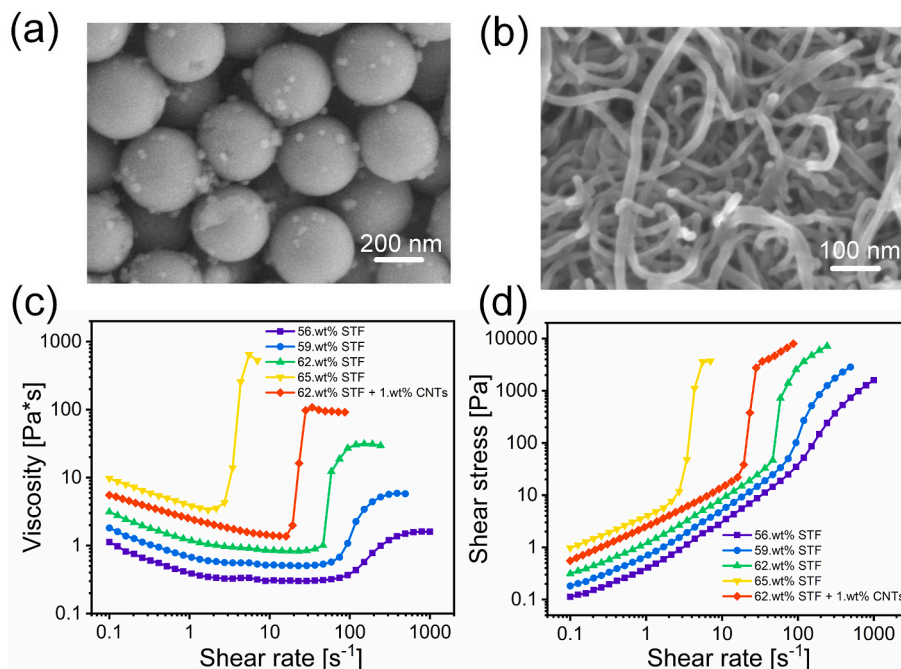The compression tests were conducted to explore the influence of

**Fig. 3.** SEM micrographs of (a) SiO₂ and (b) CNTs. The curves of the (c) viscosity vs. shear rate and (d) shear stress vs. shear rate.

STF concentration on the mechanical properties of STF/Ecoflex. Fig. 4a–d showed compression force vs. compression displacement of STF/Ecoflex with STF mass fractions of 56%, 59%, 62%, and 65% at different compression speeds. In the loading phase, it could be found that when the compression distance exceeded a critical value, the compression force increased rapidly with the increase of the compression distance, and the critical value decreased with the increase of STF concentration and compression speed. In the unloading phase, with the increase of STF concentration, the compression force decreased faster with the decrease of displacement, and when the compression force returned to zero, the residual deformation was larger. As shown in

Fig. 4e, at the same compression speed, the higher concentration of STF had, the greater the compression force the sample got. Furthermore, with the increase of loading rate, the difference of peak compression force between samples with different concentrations increased. Fig. 4f showed the energy loss of STF/Ecoflex with different concentrations of STF during a loading cycle at different speeds. The 65. wt% STF/Ecoflex dissipated the most energy at different loading speeds. In the loading stage, STF shear thickened, and its viscosity increased, resulting in an increase in compression resistance. In the unloading stage, the Ecoflex elastic shell tended to return to its original shape, and the STF dragged the elastic shell with an adhesive force stopping the recovery. The shear
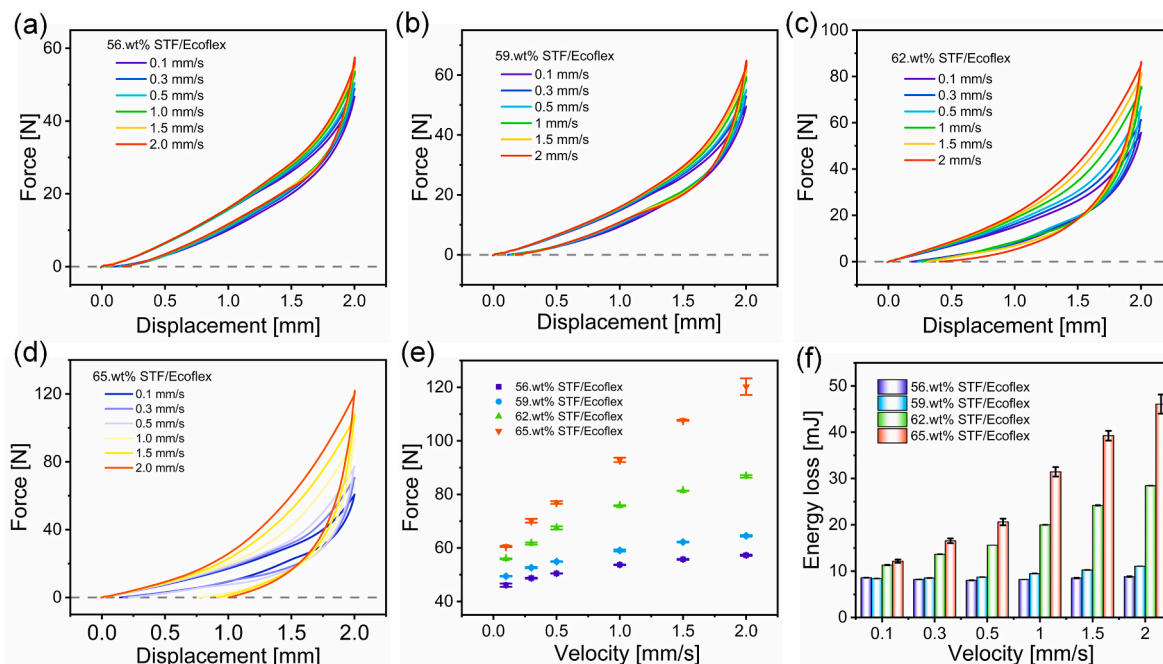


**Fig. 4.** The compression force vs. displacement at different loading speeds for (a) 56. wt% STF/Ecoflex, (b) 59. wt% STF/Ecoflex, (c) 62. wt% STF/Ecoflex and (d) 65. wt% STF/Ecoflex. (e) The peak compression forces for different samples at different pull-out speeds. (f) Energy loss of STF/Ecoflex during loading and unloading.

thickening effects became more obvious with the increase of STF concentration and compression rate, which caused more energy to be lost during the test.

### 3.2.2. Drop hammer tests

In order to explore the influence of STF concentration on STF/Ecoflex anti-impact performance under the dynamic impact, the drop hammer tests were conducted on STF/Ecoflex with different concentrations. Fig. 5a–d showed the force sensor signals vs. time of STF/Ecoflex with STF mass fractions of 56%, 59%, 62%, and 65% under the falling hammer impact. The peak force increased with the height of drop hammer. By comparing the STF/Ecoflex prepared with four concentrations of STF, it could be found that the peak force decreased and the peak force growth rate slowed down with the increase of STF concentration (Fig. 5e and f). It meant that the increase of STF concentration could enhance the attenuation of peak force. By processing the relationship between acceleration and time, the change of hammer velocity (Fig. 5g) and displacement (Fig. 5h) was obtained. The acceleration of the hammer first increased with the increase of the hammer displacement,

and then decreased (Fig. 5i). It could be found that the acceleration of the hammer at the maximum displacement was not the maximum. At the beginning of the hammerhead falling stage, the higher the concentration the STF had, the greater acceleration of the hammerhead got, while the peak acceleration was contrary to the former. It could be seen from Fig. 5j that the maximum displacement of the hammer increased with the drop height of the hammer increasing and decreased with the STF concentration increasing. As shown in Fig. 5k, with the increase of STF concentration, the rebound energy decreased. The rebound energy was lower than the impact energy, due to the viscosity dissipation caused by STF during the impact process. The energy loss was defined as the ratio of the difference between impact energy and rebound energy to impact energy. When the height of hammer drop was above 30 cm, the energy loss rate increased slightly with the increase of STF concentration (Fig. 5l). The increase of STF concentration made the shear thickening of STF more obvious and increased the resistance to the hammer head. Therefore, with the increase of STF concentration, the acceleration of the hammer head increased. When the STF/Ecoflex was compressed at the same distance, the more kinetic energy of the hammerhead was lost
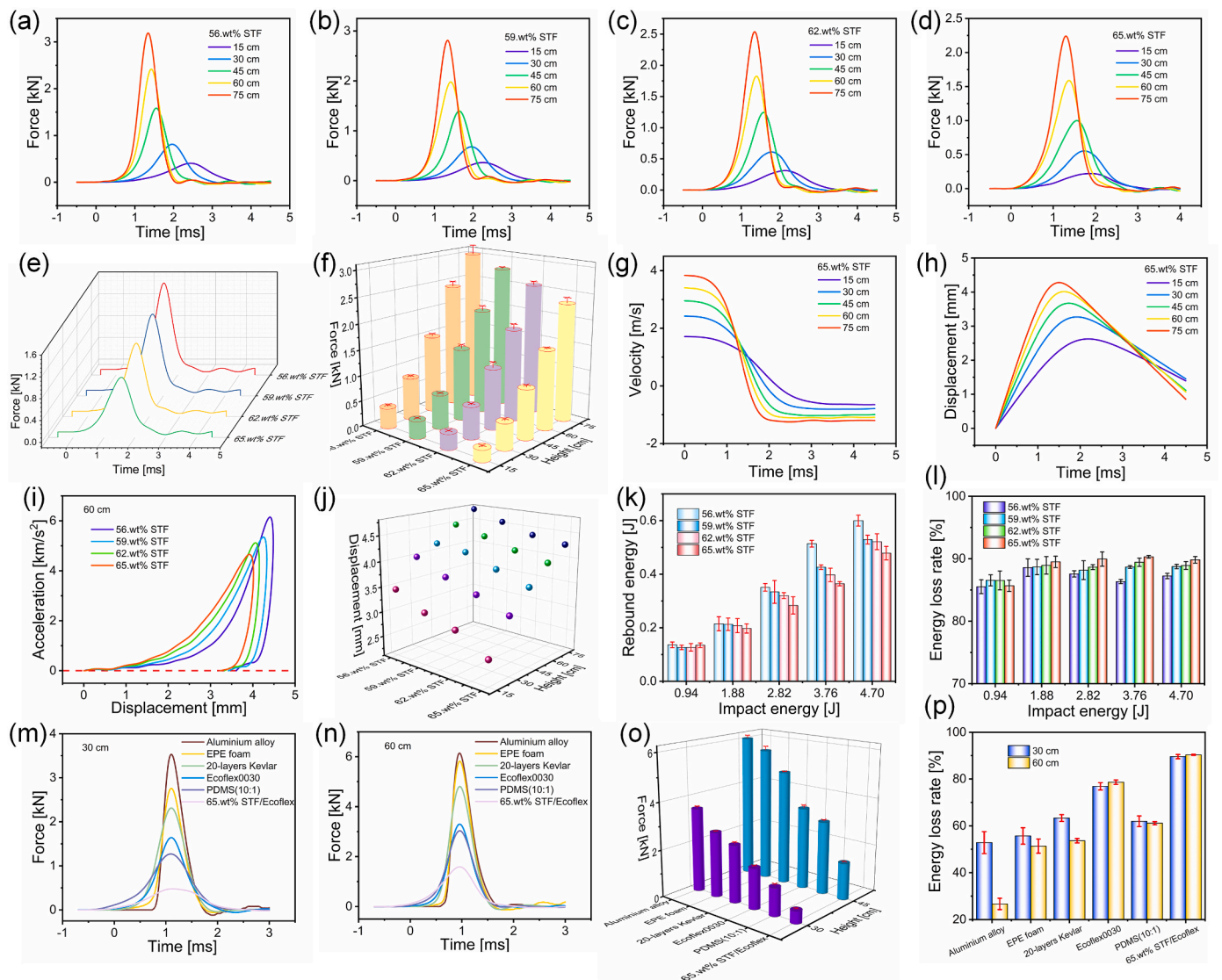


**Fig. 5.** The force vs. time curves of (a) 56 wt% STF/Ecoflex, (b) 59 wt% STF/Ecoflex, (c) 62 wt% STF/Ecoflex, and (d) 65 wt% STF/Ecoflex. (e) The force vs. time curves for different samples at the falling height of 45 cm. (f) The peak force for different samples at different falling heights. (g) The velocity vs. time curves of 65 wt% STF/Ecoflex. (h) The displacement vs. time curves of 65 wt% STF/Ecoflex. (i) The acceleration vs. displacement curves for different samples at the falling height of 60 cm. The (j) peak displacement, (k) rebound energy, and (l) energy loss rate for STF/Ecoflex with different STF concentrations. The force vs. time curves under the height of (m) 30 cm and (n) 60 cm. The (o) forces and (p) energy loss rate for different samples at different falling heights.

with higher STF concentration. When the speed of the hammerhead decayed to a certain extent, the shear thickening effect of STF weakened, resulting in a reduction of resistance to the hammerhead. At this time, the speed of the hammerhead had not decayed to zero, and it continued to fall, which caused the maximum force did not appear at the maximum compression distance. Therefore, by increasing the concentration of STF, the peak force and deformation of STF/Ecoflex could be reduced to achieve a better anti-impact effect.

To further illustrate that the STF/Ecoflex had excellent anti-impact performance, drop hammer tests were also carried out on aluminum alloy, Expanded Polyethylene (EPE) foam, 20-layers Kevlar, Ecoflex-0030, and Polydimethylsiloxane (PDMS) (10:1), respectively. Aluminum alloy and Kevlar were commonly used in body armor to absorb the kinetic energy of warheads or shrapnel, while foam and rubber were common cushioning and vibration isolation materials. Fig. 5m and n showed the time-varying relationship of impact force of different materials when the hammer head fell at a height of 30 cm and 60 cm, respectively. Compared with other materials, the force in STF/Ecoflex rose more slowly over time and STF/Ecoflex had the lowest peak force (Fig. 5o). When the height of the drop hammer increased from 30 cm to 60 cm, the increase in peak force of 65. wt% STF/Ecoflex was the smallest. As shown in Fig. 5p, when the hammer head falling height was

60 cm, the energy loss rates of aluminum alloy, EPE foam, 20-layers Kevlar, Ecoflex-0030, PDMS (10:1), and 65. wt% STF/Ecoflex were 26.7%, 51.3%, 53.7%, 78.6%, 61.1%, and 90.3%, respectively. Compared with aluminum alloy and Kevlar, the energy loss rate of 65. wt% STF/Ecoflex even increased by 63.6% and 36.6%. The above experiments verified that STF/Ecoflex had excellent dissipation ability on both force and energy, so it could be used in the body armor to effectively dissipate impact energy and prevent the harm of shock waves to the human body.

### 3.2.3. Finite element simulation

In order to explore the mechanism of the influence of STF concentration on STF/Ecoflex anti-impact performance, the process of STF/Ecoflex being impacted by falling hammer was simulated by CEL finite element method. As shown in Fig. 6a, the force of 65. wt% STF/Ecoflex on the hammer was higher than that of 62. wt% STF/Ecoflex at the beginning, but its peak force was lower than that of 62. wt% STF. The 65. wt% STF/Ecoflex dissipated more kinetic energy than 62. wt% STF/Ecoflex (Fig. 6b). It was found in both simulation and experiment that with the increase of STF concentration, the peak force decreases and the dissipated kinetic energy increases during hammer impact. The simulation results show the same trend as the experimental results. In the
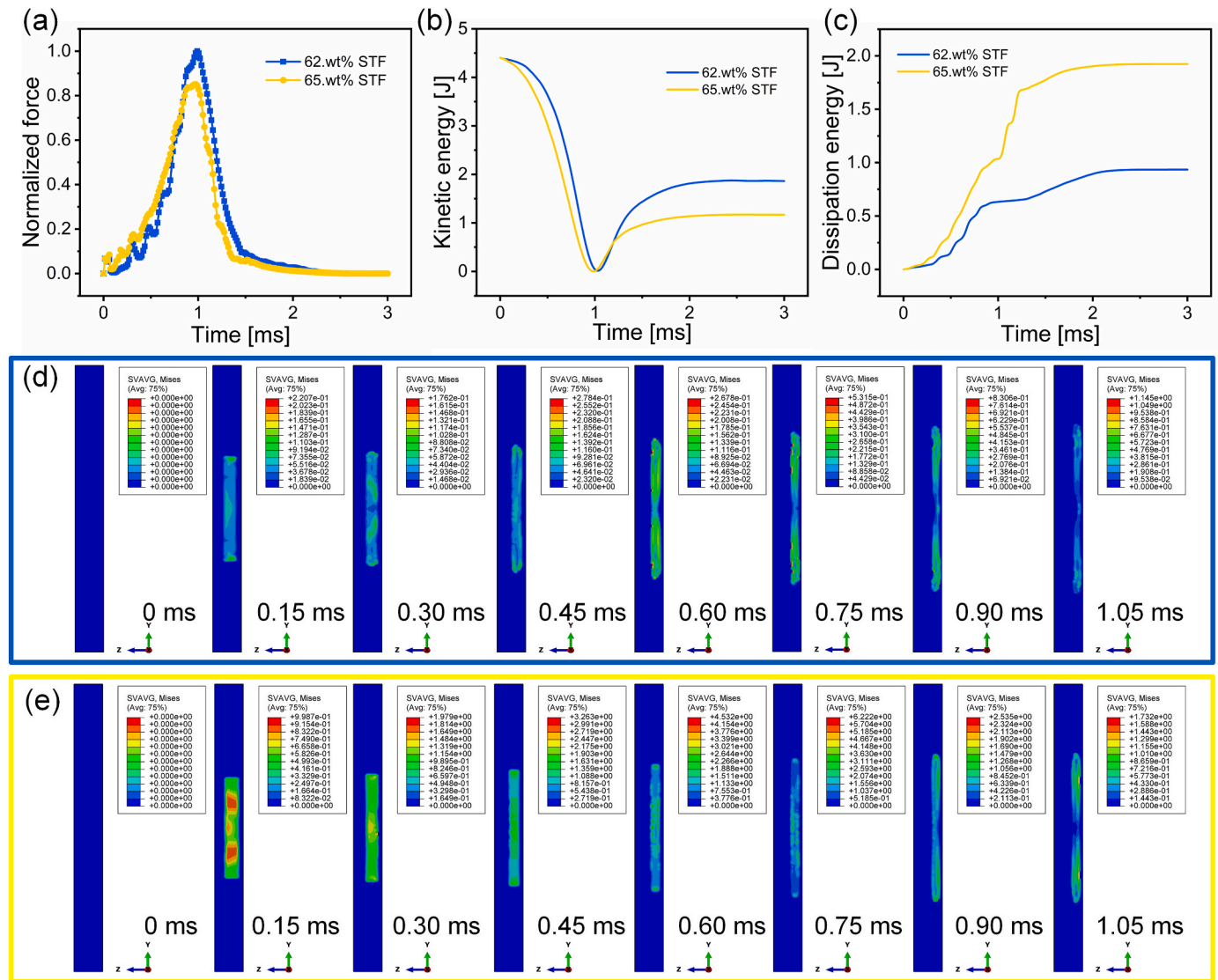


**Fig. 6.** The curves of (a) force vs. time, (b) kinetic energy vs. time, and (c) dissipation energy vs. time. Simulation results of STF SVAVG, Mises stress distribution at the central section of (d) 62. wt% STF/Ecoflex and (e) 65. wt STF/Ecoflex during impact.

impact process, the kinetic energy lost by the hammer was mainly transformed into the strain energy of the sample, the kinetic energy of the sample, and the energy lost by friction and viscosity dissipation. Fig. 6c showed the simulation results of the energy dissipated by friction and viscosity of samples at different concentrations. The energy dissipated by high concentration STF was more than that by low concentration STF. Video S1 showed stress distributions during impact for 62. wt% STF/Ecoflex and 65. wt% STF/Ecoflex elastomer shells. During the impact process, the stress at the center of the elastomer shell was the smallest. With the increase of the compression distance, the stress increased, and the stress level in the spring back process was lower than that in the compression process. Fig. 6d showed the simulation results of STF stress distribution at the central section of 62. wt% STF/Ecoflex. Within a short period of contact between the hammer head and the STF interlayer, the stress level in most areas of STF exceeded the stress level required for shear thickening. Thereafter, the stress in STF increased first and then decreased with the increase of compression distance. Compared with the stress distribution of 65 wt% STF/Ecoflex (Fig. 6e), it could be found that the stress distribution of STF with different concentrations varied with time in the same way, but the stress level of the high concentration of STF was higher than that of the low mass fraction STF at the beginning and reduced earlier during the impact. Video S2 showed the STF velocity distributions at the central sections of 62. wt%

STF/Ecoflex and 65. wt% STF/Ecoflex. As the compression distance increased, the velocity of STF increased first and then decreased. The velocity in the center of STF was the smallest. The flow velocity of different concentrations of STF had the same change pattern, but the peak flow velocity of high concentration STF was smaller and decreased earlier during the impact process. The above simulation results showed that the shear thickening occurred in STF within a short period of impact. Then, the internal stress of STF increased with the increase of STF velocity. When the hammer velocity decreased to a certain value, STF velocity decreased and the shear thickening effect weakened, resulting in the stress level of STF being reduced. With the increase of STF concentration, the shear thickening effect of STF was enhanced, which could lead to the increase of the stress level of STF and the energy dissipated by friction and viscosity.

Supplementary data related to this article can be found at https://doi.org/10.1016/j.compositesb.2022.109656.

### 3.3. C-STF/Ecoflex with sensing properties

It had been proved above that STF/Ecoflex had an excellent anti-impact performance. In addition, adding CNTs to STF could improve the shear thickening effect of STF with having the conductive for multifunctional buffering and sensing materials. Therefore, C-STF was
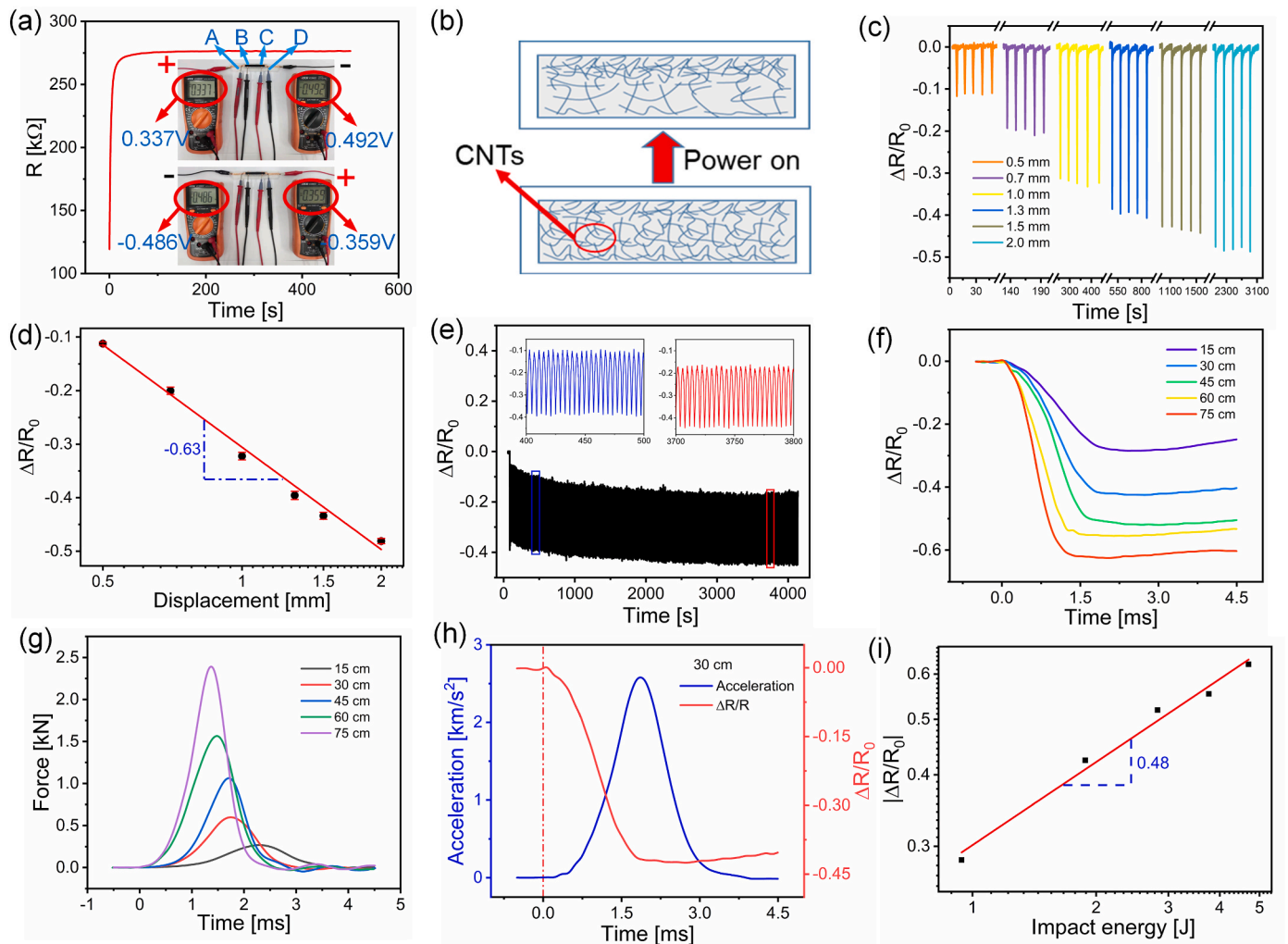


**Fig. 7.** (a) The resistance vs. time curve. (b) Diagram of CNTs distribution after power on. (c) Resistance change rate under different compression displacements. (d) The fitting curve of $\Delta R/R_0$ with compression displacement in the logarithmic coordinate system. (e) The $\Delta R/R_0$ vs. time curve under 1000 cycles of loading. The (f) $\Delta R/R_0$ and (g) force vs. time curves when the hammerhead fell from different heights. (h) The acceleration of hammerhead and $\Delta R/R_0$ vs. time curves under the falling height of 30 cm. (i) The fitting curve of $\left|\frac{\Delta R}{R_0}\right|$ with impact energy in the logarithmic coordinate system.

prepared by adding CNTs with a mass fraction of 1%–62 wt% STF, and then C-STF was encapsulated using the above method to prepare C-STF/Ecoflex. The sensor performance of C-STF/Ecoflex under different loading conditions was studied. Firstly, the resistance change of C-STF/Ecoflex at rest was tested. As shown in Fig. 7a, the initial resistance increased first and then flatten out after power-on. In order to explore the reasons for the rise of resistance, we designed an experiment as shown insert the figure of Fig. 7a. The length of STF between AB and CD was 7 mm, and the voltage between AD was 2 V. The A positive, D negative and A negative, D positive were tested respectively. The results showed that the resistance near the positive electrode would be lower than that at the negative electrode. According to the experimental results, the possible reason (Fig. 7b) for the phenomenon in Fig. 7a was given here. After electrification, CNTs with negatively charged gathered to the anode area under the action of electric potential difference, causing uneven distribution of carbon nanotubes within the STF, thus causing the C-STF/Ecoflex resistance increased. As CNTs aggregated, the repulsion of CNTs with the same charge also increased, the resistance rose at a slower pace. Eventually, repulsive force and the traction reached equilibrium, and resistance no longer changed. Before the test, a voltage was applied to the sample until the resistance of the sample reached a stable value, at which point the resistance was recorded as the initial resistance $R_0$. The resistance change was defined as $\Delta R = R - R_0$. As shown in Fig. 7c, the sensing performance of C-STF/Ecoflex at a compression displacement of 0.5–2 mm and loading rate of 1 mm/s was studied. The test was repeated five times at each compression displacement. With the increase of compression displacement, the electrical response of C-STF/Ecoflex became obvious. In addition, it was found that the peak resistance variation had a linear relationship with the compression distance in the logarithmic coordinate system, and its slope was −0.63 (Fig. 7d). Since the stability of the sensor was critical in practical applications, 1000 continuous compression tests were performed on the sensor at a compression speed of 1 mm/s and a maximum compression distance of 1 mm. As shown in Fig. 7e, with the increase of the number of cycles, the resistance first decreased and then gradually reached equilibrium. The flow of STF dispersed CNTs more evenly during the cycle, thus causing a reduction in resistance. Cyclic compression test results showed that the C-STF/Ecoflex had good sensitivity and stability, and could be used for sensors.

Then, C-STF/Ecoflex was subjected to drop hammer impact tests with drop hammer heights ranging from 15 cm, 30 cm, 45 cm, and 60 cm–75 cm, respectively. Fig. 7f showed the variation relation of $\Delta R/R_0$ with time when the drop hammer fell from different heights. It could be found that with the increase of the drop hammer height, the change of resistance in the impact process accelerated and the peak value change rate increased. As could be seen from Fig. 7g, when the hammer head dropped from 75 cm to impact C-STF/Ecoflex, the peak force was 2.4 kN. However, when the hammer head dropped from 75 cm to impact 62. wt % STF/Ecoflex, the peak force was 2.6 kN (Fig. 5c). The above phenomenon indicated that the addition of CNTs helped to improve the dissipation capacity of STF/Ecoflex on the impact force. Fig. 7h showed the time-varying relationship between the acceleration and resistance of the falling hammer in the impact process. It could be found that signals were almost simultaneously generated by the resistance of C-STF/Ecoflex and the acceleration sensor on the hammer head, indicating that C-STF/Ecoflex had a fast response speed. According to the theory of Boland [43]:

$$\left|\frac{\Delta R}{R_0}\right| \propto \left(E_{mgh}\right)^k \tag{2}$$

where $E_{mgh}$ was the impact energy, and $k$ was a constant related to the structure of the conductive network. The fitting line was shown in Fig. 7i, the $k$ was 0.48, and the standard error of the fitting result was 0.03, indicating that the resistance change behavior under dynamic impact was directly related to impact energy. The above experiments

verified the C-STF/Ecoflex could be used as a sensor with protective performance under impact conditions.

### 3.4. The versatile wearable C-STF/Ecoflex/Kevlar responds to external stimuli

Kevlar fiber with high tensile modulus and ideal bending deformation was a candidate material for the development of new portable sensors with sensing and protection properties. Therefore, in order to develop multi-functional protective clothing with an anti-impact effect, a wearable C-STF/Ecoflex/Kevlar was developed by stitching C-STF/Ecoflex on the surface of Kevlar fabric. Then, the impact effect under ballistic impact was tested. Projectiles with different velocities were used to impact the sample, and the resistance changes of the sample were recorded by an oscilloscope (Fig. 8a). It could be found that when the projectile touched the sample, the resistance of the sample decreased sharply, and the variation of sample resistance increased with the increase of the projectile velocity (Fig. 8b and c). Eq. (2) was used to fit the relationship between $\Delta R/R_0$ and impact energy, and the results were shown in Fig. 8d. As expected, the data followed a power law with k ~ 0.45. The fitting result was quite reasonable with a standard error of 0.04, indicating that the resistance behavior in ballistic impact conditions was related to impact energy directly as the theory depicted. Due to its light weight and high flexibility, the C-STF/Ecoflex/Kevlar array was designed to be wearable. The flexible array (Fig. 8e) could be comfortably worn on the human arm (Fig. 8f), leg (Fig. 8g), knee (Fig. 8h), and waist (Fig. 8i). By assembling the four arrays (Fig. 8j) together, a large scale area could be obtained. In addition, smart clothing electronics had demonstrated their versatility in sensing various external stimuli. Under impact (Fig. 8k) and compression (Fig. 8l and m), the array could also accurately monitor position and force distribution through pixel $\Delta R/R_0$. The maximum $\Delta R/R_0$ signals under shock and compression were −0.44, −0.07, and −0.11, respectively. These signals were very stable, showing a reliable sensing effect for various dangerous stimuli. To this end, the C-STF/Ecoflex/Kevlar was a smart wearable device with protective properties.

### 4. Conclusion

In this paper, the STF/Ecoflex was obtained by encapsulating STF in Ecoflex-0030. Then compression tests and drop hammer tests were carried out to explore the effect of STF concentration on the anti-impact properties of composites. The increase of STF concentration improved the dissipative ability of STF/Ecoflex to peak force and reduced the deformation of STF/Ecoflex, which was beneficial to the anti-impact performance of STF/Ecoflex. Compared with other materials of the same volume, the peak force of 65. wt% STF/Ecoflex was the lowest. Furthermore, the energy loss rate of 65. wt% STF/Ecoflex could reach 90.3%, which was 63.6% and 36.6% higher than aluminum alloy and Kevlar materials, respectively. The mechanism was studied by numerical simulation. Within a short period time after STF/Ecoflex was impacted, the shear thickening occurred in STF and the viscosity increased, which caused hammer drop resistance increased. When the hammer speed was reduced to a certain extent, the viscosity of STF decreased, preventing further increase of resistance. The increase of STF concentration improved the shear thickening effect of STF, which improved the internal stress of STF and was helpful to reduce the peak force and hammer displacement. Then, the C-STF/Ecoflex with good impact sensing function was obtained by adding CNTs into STF. Finally, the C-STF/Ecoflex/Kevlar was prepared by stitching C-STF/Ecoflex on the surface of Kevlar fabric, which could be used in multi-functional anti-impact wearable devices.

### Author statement

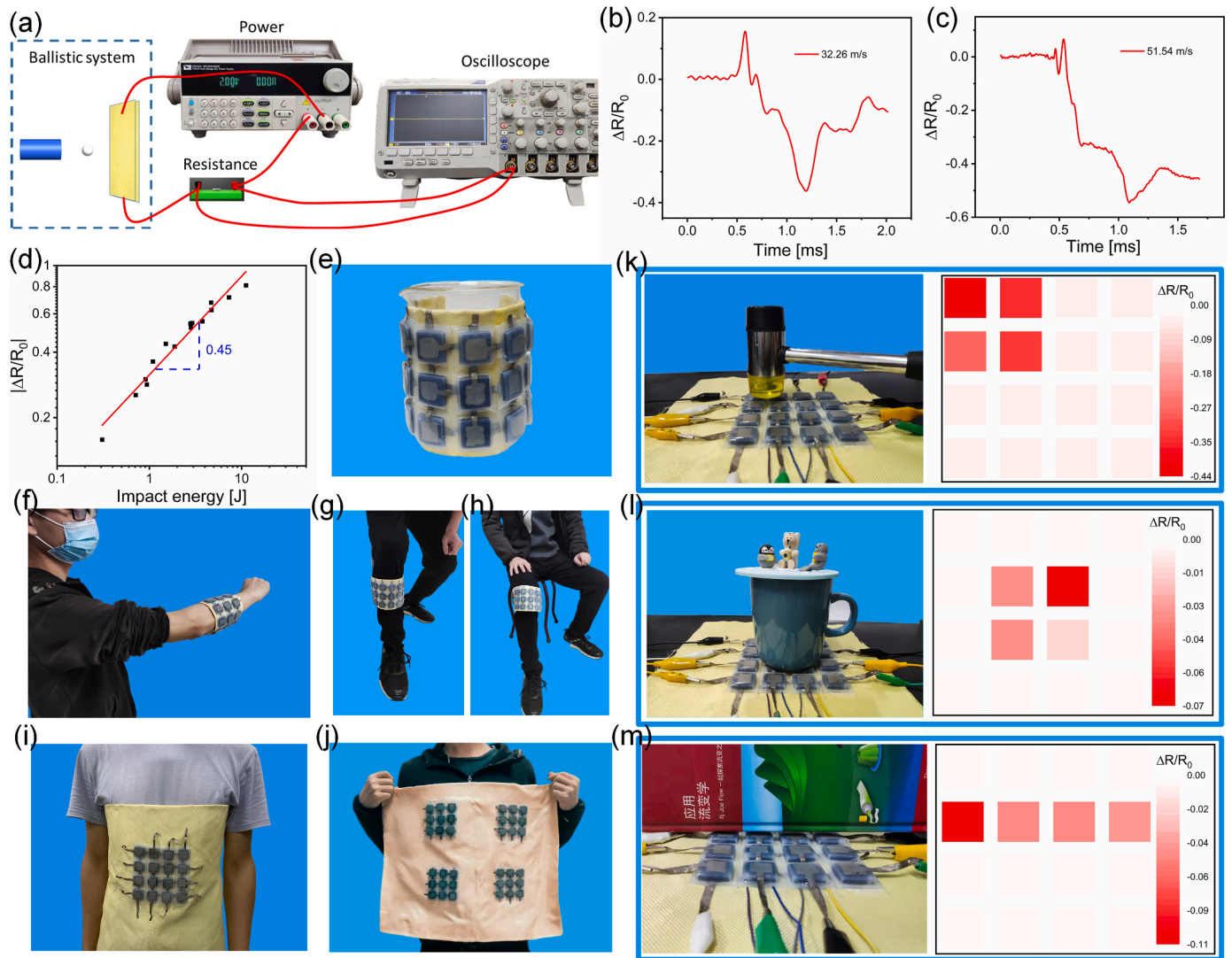Junshuo Zhang: Conceptualization, Investigation, Writing - Original

**Fig. 8.** (a) Schematic of the system for recording the variation of C-STF/Kevlar resistance during the high-speed impact. The curves of the resistance signal of C-STF/Kevlar under (b) 32.26 m/s and (c) 51.54 m/s. (d) The fitting curve of $|\frac{\Delta R}{R_0}|$ with impact energy in the logarithmic coordinate system. Shape programmable photographs of C-STF/Ecoflex/Kevlar device: (e) bendable, (f) worn on arm, (g) worn on leg, (h) worn on knee, (i) the overlying one provided higher protection effect, and (j) the arrays were integrated into one pad with larger protection area. Photographs of 4 × 4 sensor array in different regions under different loading conditions and the corresponding resistance variation distribution: (k) hammer, (l) water glass, and (m) book.

Draft.

Yu Wang: Methodology, Funding acquisition, Writing - review & editing.

Huaxia Deng: Investigation.

Jianyu Zhou: Investigation, Formal analysis.

Shuai Liu: Investigation.

Jianpeng Wu: Investigation.

Min Sang: Formal analysis.

Xinglong Gong: Supervision, Project administration, Resources, Funding acquisition, Writing - review & editing.

## Declaration of competing interest

The authors declare that they have no known competing financial interests or personal relationships that could have appeared to influence the work reported in this paper.

## Acknowledgments

## Appendix A. Supplementary data

Supplementary data to this article can be found online at https://doi.org/10.1016/j.compositesb.2022.109656.

## References

[1] Zwingmann L, Hoppstock M, Goldmann JP, Wahl P. The effect of physical training modality on exercise performance with police-related personal protective equipment. Appl Ergon 2021;93:103371.

[2] Braga F, Lopes P, Oliveira M, Monteiro S, Lima E. Thickness assessment and statistical optimization of a 3-layered armor system with ceramic front and curaua fabric composite/aluminum alloy backing. Compos B Eng 2019;166:48–55.

[3] Takata Y, Matsuoka S, Okumura N, Iwamoto K, Takahashi M, Uchiyama E. Standing balance on the ground -The influence of flatfeet and insoles. J Phys Ther Sci 2013;25(12):1519–21.

[4] Jiang W, Gong X, Wang S, Chen Q, Zhou H, et al. Strain rate-induced phase transitions in an impact-hardening polymer composite. Appl Phys Lett 2014;104 (12):121915.

[5] Majumdar A, Butola B, Srivastava A. An analysis of deformation and energy absorption modes of shear thickening fluid treated Kevlar fabrics as soft body armour materials. Mater Des 2013;51:148–53.

[6] Decker M, Halbach C, Nam C, Wagner N, Wetzel E. Stab resistance of shear thickening fluid (STF)-treated fabrics. Compos Sci Technol 2007;67(3–4):565–78.

[7] Bajya M, Majumdar A, Butola B, Verma S, Bhattacharjee D. Design strategy for optimising weight and ballistic performance of soft body armour reinforced with shear thickening fluid. Compos B Eng 2020;183:107721.

[8] Barnes HA. Shear-thickening (Dilatancy) in suspensions of non-aggregating solid particles dispersed in Newtonian liquids. J Rheol 1989;33(2):329–66.

[9] Cheng X, McCoy JH, Israelachvili JN, Cohen I. Imaging the microscopic structure of shear thinning and thickening colloidal suspensions. Science 2011;333(6047): 1276–9.

[10] Cao S, Wang Y, Pang H, Zhang J, Wu Y, et al. Shear jamming onset in dense granular suspensions. J Rheol 2021;65(3):419–26.

[11] Gurgen S, Sofuoglu MA. Vibration attenuation of sandwich structures filled with shear thickening fluids. Compos B Eng 2020;186:107831.

[12] Smith MI, Besseling R, Cates ME, Bertola V. Dilatancy in the flow and fracture of stretched colloidal suspensions. Nat Commun 2010;1:114.

[13] Jiang W, Gong X, Xuan S, Jiang W, Ye F, et al. Stress pulse attenuation in shear thickening fluid. Appl Phys Lett 2013;102(10):101901.

[14] Jerome JJS, Vandenberghe N, Forterre Y. Unifying impacts in granular matter from quicksand to cornstarch. Phys Rev Lett 2016;117(9):098003.

[15] Gürgen S, Sert A. Polishing operation of a steel bar in a shear thickening fluid medium. Compos B Eng 2019;175:107127.

[16] Gürgen S, Sofuoglu MA. Integration of shear thickening fluid into cutting tools for improved turning operations. J Manuf Process 2020;56:1146–54.

[17] Lin K, Liu H, Wei M, Zhou A, Bu F. Dynamic performance of shear-thickening fluid damper under long-term cyclic loads. Smart Mater Struct 2019;28(2):025007.

[18] Gürgen S, Sofuoglu MA. Smart polymer integrated cork composites for enhanced vibration damping properties. Compos Struct 2021;258:113200.

[19] Li T, Dai W, Wu L, Peng H, Zhang X, Shiu B, et al. Effects of STF and fiber characteristics on quasi-static stab resistant properties of shear thickening fluid (STF)-impregnated UHMWPE/Kevlar composite fabrics. Fibers Polym 2019;20(2): 328–36.

[20] Wang Q, Sun R, Yao M, Chen M, Feng Y. The influence of temperature on inter-yarns fictional properties of shear thickening fluids treated Kevlar fabrics. Composer Part A Appl S 2019;116:46–53.

[21] Cao S, Chen Q, Wang Y, Xuan S, Jiang W, Gong X. High strain-rate dynamic mechanical properties of Kevlar fabrics impregnated with shear thickening fluid. Compos Appl Sci Manuf 2017;100:161–9.

[22] Manukonda BH, Chatterjee VA, Verma SK, Bhattacharjee D, Biswas I, Neogi S. Rheology based design of shear thickening fluid for soft body armor applications. Period Polytech - Chem Eng 2020;64(1):75–84.

[23] Ghosh A, Majumdar A, Butola BS. Role of surface chemistry of fibres additives on rheological behavior of ceramic particle based Shear Thickening Fluids. Ceram Int 2018;44(17):21514–24.

[24] Tan ZH, Li WH, Huang W. The effect of graphene on the yarn pull-out force and ballistic performance of Kevlar fabrics impregnated with shear thickening fluids. Smart Mater Struct 2018;27(7):075048.

[25] Park JL, Yoon BI, Paik JG, Kang TJ. Ballistic performance of p-aramid fabrics impregnated with shear thickening fluid; Part I - effect of laminating sequence. Textil Res J 2012;82(6):527–41.

[26] Arora S, Majumdar A, Butola BS. Soft armour design by angular stacking of shear thickening fluid impregnated high-performance fabrics for quasi-isotropic ballistic response. Compos Struct 2020;233:111720.

[27] Gürgen S, Fernandes FA, Sousa RJ, Kushan MC. Development of eco-friendly shock-absorbing cork composites enhanced by a non-Newtonian fluid. Appl Compos Mater 2021;28(1):165–79.

[28] Sheikhi MR, Gürgen S. Anti-impact design of multi-layer composites enhanced by shear thickening fluid. Compos Struct 2022;279:114797.

[29] Lin M, Lou C, Lin J, Lin T, Lin J. Mechanical property evaluations of flexible laminated composites reinforced by high-performance Kevlar filaments: tensile strength, peel load, and static puncture resistance. Compos B Eng 2019;166: 139–47.

[30] Lee YS, Wetzel ED, Wagner NJ. The ballistic impact characteristics of KevlarÒ woven fabrics impregnated with a colloidal shear thickening fluid. J Mater Sci 2003;38(13):2825–33.

[31] Mawkhlieng U, Majumdar A. Deconstructing the role of shear thickening fluid in enhancing the impact resistance of high-performance fabrics. Compos B Eng 2019; 175:107167.

[32] Khodadadi A, Liaghat G, Vahid S, Sabet AR, Hadavinia H. Ballistic performance of Kevlar fabric impregnated with nanosilica/PEG shear thickening fluid. Compos B Eng 2019;162:643–52.

[33] Trung TQ, Lee NE. Flexible and stretchable physical sensor integrated platforms for wearable human-activity monitoring and personal healthcare. Adv Mater 2016;28 (22):4338–72.

[34] Fernandez RE, Umasankar Y, Manickam P, Nickel JC, Iwasaki LR, Kawamoto BK, et al. Disposable aptamer-sensor aided by magnetic nanoparticle enrichment for detection of salivary cortisol variations in obstructive sleep apnea patients. Sci Rep 2017;7(1):17992.

[35] Kuang J, Dai Z, Liu L, Yang Z, Jin M, Zhang Z. Synergistic effects from graphene and carbon nanotubes endow ordered hierarchical structure foams with a combination of compressibility, super-elasticity and stability and potential application as pressure sensors. Nanoscale 2015;7(20):9252–60.

[36] Vilarinho D, Theodosiou A, Leitão C, Leal-Junior AG, Domingues MdF, et al. POFBG-embedded cork insole for plantar pressure monitoring. Sensors 2017;17 (12):2924.

[37] Wu J, Wang J, Ling Y, Xu H. An advanced hybrid technique of dcs and jsrc for telemonitoring of multi-sensor gait pattern. Sensors 2017;17(12):2764.

[38] Qin J, Guo B, Zhang L, Wang T, Zhang G. Soft armor materials constructed with Kevlar fabric and a novel shear thickening fluid. Compos B Eng 2020;183:107686.

[39] Liu M, Zhang S, Liu S, Cao S, Wang S, et al. CNT/STF/Kevlar-based wearable electronic textile with excellent anti-impact and sensing performance. Compos Appl Sci Manuf 2019;126:105612.

[40] Wang S, Liu S, Zhou J, Li F, Li J, et al. Advanced triboelectric nanogenerator with multi-mode energy harvesting and anti-impact properties for smart glove and wearable e-textile. Nano Energy 2020;78:105291.

[41] Steck D, Qu J, Kordmahale SB, Tscharnuter D, Muliana A. Mechanical responses of Ecoflex silicone rubber: compressible and incompressible behaviors. J Appl Polym Sci 2019;136(5):47025.

[42] Sen S, Bin J, Shaw A, Deb A. Numerical investigation of ballistic performance of shear thickening fluid (STF)-Kevlar composite. Int J Mech Sci 2019;164:105174.

[43] Boland CS, Khan U, Ryan G, Barwich S, Charifou R, Harvey A, et al. Sensitive electromechanical sensors using viscoelastic graphene-polymer nanocomposites. Science 2016;354(6317):1257–60.